

## Wave–Tide Interaction for a Strongly Modulated Wave Field

ALLISON HO,<sup>a</sup> SOPHIA MERRIFIELD,<sup>a</sup> AND NICK PIZZO<sup>a</sup>

<sup>a</sup> *Scipps Institution of Oceanography, University of California, San Diego, La Jolla, California*

(Manuscript received 8 August 2022, in final form 2 November 2022)

**ABSTRACT:** Observations from Coastal Data Information Program (CDIP) moored buoys off the coast of Florida reveal tidally driven wave–current interactions that modify significant wave heights by up to 25% and shift peak periods by up to a second. A case study at Fernandina Beach, Florida, shows surface waves steepening on following tidal currents and becoming less steep on opposing tidal currents, with the largest modulations occurring in the long-period swell band. To better understand tidal modulations as a function of the phase of the tide, we use simplified analytical and numerical solutions to the equations of geometrical optics and conservation of wave action under the assumption of a one-dimensional tide acting as a progressive shallow-water wave. The theoretical frameworks allow us to identify parameters that characterize the magnitude of variation in surface waves due to tidally induced currents and changes in water depth. We compute modulations to the omnidirectional and directional wave spectrum (between 0.05 and 0.15 Hz), as well as characteristic bulk parameters such as significant wave height and peak period. The theory is corroborated using directional wave and surface current observations from the Fernandina Beach CDIP station (located in water of average depth of 16 m). We find that the numerical results reproduce the observed wave modulations due to tidal currents and changes in water depth. Specifically, surface waves traveling in the direction of the tide are strongly modulated, and the relative speeds between the tide and surface waves set the sign and magnitude of these modulations. Given knowledge of tidal currents, water-depth variations, and wave climatology, theoretical and numerical predictions may be used to provide both statistical and instantaneous estimates of wave-height variations due to tides. Because operational forecasts and nowcasts do not routinely include tides or currents, these findings can help to accurately represent nearshore surface wave variability.

**KEYWORDS:** Currents; Tides; Oceanic waves

### 1. Introduction

Understanding the tidal influence on surface waves is important for maritime safety and navigation, coastal management and adaptation strategies, sediment transport, air–sea fluxes, accurate wave predictions for surf and hazard forecasts, and interpretation of measurements of the ocean surface. Some of the earliest theoretical work on wave–current interaction was motivated by the influence of tides; Bristol Channel pilots saw the roughest seas at the end of the flood tide (Unna 1942), and the interaction of waves and tidal currents off the coast of Cornwall, England, was considered in an early study by Barber (1949). The tidal influence on coastal wave climates has been reported in numerous studies. For example, in shallow continental shelves, wave-height modulations of up to 20%–50% have been attributed to tidal currents (Tolman 1990; Wang and Sheng 2018; Lewis et al. 2019).

When waves interact with currents, their amplitudes and phase may be modulated, which can lead to strong steepness modulations (Rasche and Ardhuin 2013) and in some cases enhanced wave breaking (Romero et al. 2017; Vrećica et al. 2022). Although the study of wave–current interaction is well developed (Longuet-Higgins and Stewart 1960; Phillips 1966; Bretherton and Garrett 1968; Peregrine 1976; Wolf and Prandle

1999; Cavaleri et al. 2007), it is only recently that multiple varieties of observations and models are being integrated and compared (Bôas et al. 2019). There is evidence of surface waves interacting with currents at a broad range of spatial and temporal scales from the submesoscale (Phillips 1984; Baschek 2005; Romero et al. 2017, 2020; Vrećica et al. 2022) to large-scale circulation (Holthuijsen and Tolman 1991; Ardhuin et al. 2017; Barnes and Rautenbach 2020). A recent study has shown that wave modulation by currents accounts for more than 75% of the spatial variability of wave heights at scales of 100 km or shorter in wave models; a significant portion of the variability in significant wave height is due to refraction over current gradients (Ardhuin et al. 2017). Additionally, many open questions still remain about the two-way coupling between waves and currents (Bühler and Jacobson 2001; Bühler and McIntyre 2005; Pizzo and Salmon 2021). Wave models require high-resolution current fields to fully resolve wave-height gradients due to currents (Marechal and Ardhuin 2021). Without currents, models may not accurately predict spectral peaks, swell arrival times, spatial gradients, and energy of waves.

The interaction of waves and currents typically is examined in the framework of conservation of wave action (Longuet-Higgins and Stewart 1960; Bretherton and Garrett 1968) and geometrical optics (e.g., Peregrine 1976). Wave action, or the wave energy divided by its intrinsic frequency, is the conserved quantity in this system, as the waves and currents may freely exchange momentum and energy. Geometrical optics constrains kinematic properties of the wave field, such as the Doppler shift of the wave frequency due to currents and the resulting implications on wave refraction. A canonical textbook example

 Denotes content that is immediately available upon publication as open access.

Corresponding author: Allison Ho, aho@ucsd.edu

considers a uniform wave field on a steady but spatially nonuniform opposing current, which leads to wave steepening on opposing currents (Phillips 1966; Mei 1992).

Tidal environments, however, are neither steady nor homogeneous in space or time. Tides propagate as shallow-water waves around ocean basins, generating associated currents and changes in water level that we see at the shore. The relatively higher-frequency surface gravity waves propagate in this inhomogeneous and unsteady medium, requiring more complex numerical wave models (Tolman 1991; Booij et al. 1999). The unsteadiness of the tides leads to modulations to the wave field that contradict our intuition based on waves interacting with steady currents. In particular, several studies have presented observations of wave heights *increasing* on following tidal currents (Gemrich and Garrett 2012; Wang and Sheng 2018), contrasting the behavior seen for steady currents. Observations of the relative phase between the tidal currents and minima and maxima of the wave energy (i.e., the significant wave height) have been hypothesized to be due to refraction, wave dissipation (Davidson et al. 2008), relative wind (Ardhuin et al. 2012), or water-depth effects. Here we seek a simple understanding for how changes in currents and water depths due to tides impact wave frequencies and amplitudes of an incoming spectrum of waves.

In this study, we present observations of tidally driven wave-current interaction. Wave measurements at a moored buoy at Fernandina Beach, Florida, show strong semidiurnal variability, modifying significant wave heights and peak periods up to 25% over a tidal cycle. The period of modulation (12.42 h) suggests influence from currents and water-depth variations associated with the semidiurnal tide. In particular, these observations also show that waves increase in steepness on following currents. We demonstrate how the observed modulations can be described in a theoretical framework in which we model the tide as a linear shallow-water surface gravity wave so the wave-tide interaction may be written as a long wave-short wave interaction (Longuet-Higgins and Stewart 1962). In section 2, we describe the observations from the Coastal Data Information Program (CDIP) Fernandina Beach station; in section 3, we describe the two approaches used to explain the observed phenomena. Next, in section 4, we compare the models with the observations, and in sections 5 and 6 we summarize the results and implications.

## 2. Data

CDIP at the Scripps Institution of Oceanography operates a network of moored Datawell Waverider directional wave buoys to monitor wave conditions in coastal regions of the Atlantic and Pacific Oceans. CDIP's operational buoy network has been used to assist coastal management and hazards mitigation, support maritime operations, and inform numerous scientific programs (e.g., Hanson et al. 2009; O'Reilly et al. 1996; Merrifield et al. 2021). Accelerometers measure the vertical and horizontal acceleration of the buoy at 2.56 Hz. Statistical wave parameters, wave energy spectra, and the first four directional moments are computed every half hour using 17 overlapping 200-s windows (50% overlap; Hann window) of the raw displacements. This provides spectral resolution from 0.04 to 1 Hz. The half-hourly wave data are transmitted from the buoys via Iridium satellite

and are publicly available online (cdip.ucsd.edu). Directional spectra are estimated via the maximum entropy method (MEM; Kuik et al. 1988).

This study examines wave observations from the CDIP buoy station 132 (CDIP132), located offshore of Fernandina Beach in 16-m water depth, shown in Fig. 1. In September of 2020, CDIP132 was redeployed with a Datawell Waverider 4 (DWR4; Datawell B.V. 2021) equipped with an acoustic current meter to provide direct observations of surface currents. In the hull of DWR4, three acoustic transducers with 2-MHz acoustic frequency measure the current velocity between 0.5 and 1.75 m from the surface. CDIP132 surface currents throughout the first year of deployment (1 August 2020–1 August 2021) are on average  $0.23 \text{ m s}^{-1}$ . Surface currents are tidally dominated (see harmonic analysis in Table 1 for dominant tidal constituents), in agreement with the climatology observed in a 2006/07 U.S. Army Corps of Engineers study (McArthur and Parsons 2009).

The wave climate off the east coast of Florida is dominated by seasonal local swells from nor'easters and hurricanes and trade winds. At CDIP132 from 1 August 2020 to 1 August 2021, the dominant wave direction is from the east ( $105^\circ$ ) with 8.8-s average peak periods and 0.93 m average significant wave heights, but wave heights have been measured up to 3.3 m during extreme events. Onshore southeast diurnal winds that peak in the afternoon with average maximum wind speeds up to  $6 \text{ m s}^{-1}$  are not coherent with wave parameters. Figure 1 shows an overview of observations from CDIP132, collected over 4 days in August of 2020. Clear semidiurnal signals are apparent in the spectral and bulk parameters (Figs. 1c–e). Spectral analysis of one year of concurrent bulk wave and current and water-level data was performed by taking the fast Fourier transform of the demeaned and detrended time series over 60-day half-overlapping segments. Spectra of surface currents (Fig. 2f) and water levels (Fig. 2g) show strong peaks at the principal lunar constituent M2, consistent with the dominant constituents of the observed currents and wave variations, shown in Table 1. Frequency spectral analysis on the swell significant wave height  $H_{s,\text{swell}}$  (Fig. 2c), defined as the significant wave height  $H_s = 4\sqrt{E}$  (where  $E$  is the surface elevation variance) in the frequency range of 0.05 to 0.18 Hz, shows that the primary period of oscillation is 12.42 h, the M2 semidiurnal period, suggesting that the wave variations are due to a tidally driven process. The swell peak period  $T_{p,\text{swell}}$  and swell directional spread  $\sigma_{\text{swell}}$  also have primary dominant peaks at the M2 tidal frequency (not shown). Tidal variations in significant wave height, peak period, and directional spread have dominant periods at the M2 tidal frequency (Table 1). Nearly 90% of the tidal variability in the significant wave height can be attributed to the M2 tide. Because of the well-documented tidal currents, fixed wave direction, and strong observed modulations, this location was well suited for a case study of wave-tide interaction.

Tidal currents and water levels are measured at the nearby NOAA Tides and Currents Station 8720030 in the Fernandina Beach port on the Amelia River, available at tidesandcurrents.noaa.gov. Barotropic tidal currents and water levels are predicted at the buoy location using the data-assimilated global tidal model TPXO 9 and Tide Model Driver 2.5 (Egbert and Erofeeva 2002;

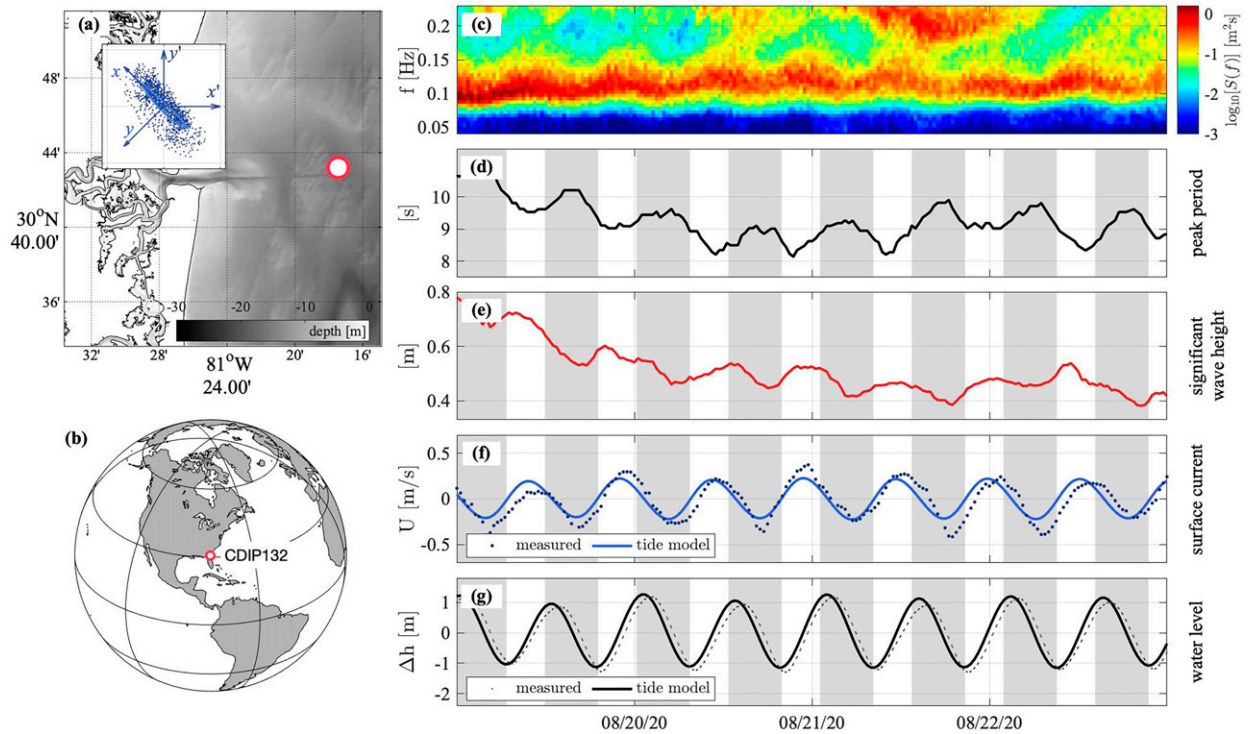


FIG. 1. (a),(b) Location and measurements from the CDIP Datawell Waverider directional wave buoy CDIP132 used to develop and corroborate the model: a 10-day sample of wave measurements including (c) spectra, (d) peak period, (e) significant wave height, (f) surface currents projected onto the peak wave direction, and (g) change in water depth from a tidal model and measured at a nearby NOAA tide gauge. The tidal current ellipse is shown inlaid in (a) with the Earth coordinates axes ( $x'$ ,  $y'$ ) and current coordinates axes ( $x$ ,  $y$ ) labeled. Gray boxes are shaded every 6.2 h to highlight the change in wave parameters in terms of the phase of the tide.

Erofeeva et al. 2020). Dominant constituents given by the tide model for the buoy location and corresponding percent variance of the observed currents and wave variations explained by each constituent are shown in Table 1. At CDIP132, the M2 tidal

TABLE 1. First five dominant tidal constituents (M2, N2, S2, K1, and O1) for Fernandina Beach (30°42'33.1"N, 81°17'31.2"W) from the global tidal model TPXO 9 and Tide Model Driver 2.5 (Egbert and Erofeeva 2002; Erofeeva et al. 2020). The corresponding periods (h) for these five constituents are 12.42, 12.66, 12.00, 23.93, and 25.82, respectively. The corresponding amplitudes (m) are 0.85, 0.19, 0.14, 0.11, and 0.07, respectively. For each constituent, the percent variance was calculated over two years via a least squares fit for each of the observed variables. The observed variables include surface currents  $u_{\text{obs}}$  and  $v_{\text{obs}}$  and the changes in swell significant wave height  $\Delta H_{s,\text{swell}}$ , swell peak period  $\Delta T_{p,\text{swell}}$ , and swell directional spread  $\Delta \sigma_{\text{swell}}$ . A 2-day, high-pass filter was applied to each observed variable. The total percent variance is calculated from the fit to all five dominant tidal constituents.

Obs variable	Percent variance (modeled/observed; %)					Total
	M2	N2	S2	K1	O1	
$u_{\text{obs}}$ ( $\text{m s}^{-1}$ )	63.07	3.17	2.48	0.78	0.26	69.88
$v_{\text{obs}}$ ( $\text{m s}^{-1}$ )	56.09	3.36	2.08	0.89	0.39	62.96
$\Delta H_{s,\text{swell}}$ (%)	13.00	0.80	0.32	0.21	0.15	14.50
$\Delta T_{p,\text{swell}}$ (%)	6.26	0.44	0.30	0.18	0.18	7.38
$\Delta \sigma_{\text{swell}}$ (%)	4.52	0.54	0.39	0.53	0.17	6.17

component of the observed surface currents shows strong agreement with the tide model (Fig. 2a). In the continental shelf region of the mid-Atlantic Bight, the tides and modulations to the waves are dominated by the M2 tidal component, shown in Fig. 2, which allows us to approximate the tide with a single tidal frequency. Nearly 70% of the variance in the observed surface currents is tidal, and the majority of that is attributed to the M2 constituent (Table 1). Additionally, currents flow predominantly in the north–northwest and south–southeast direction, as shown in Fig. 1a. The current ellipse is oriented along 135°, or 45° to the shore, with a semimajor axis of  $0.28 \text{ m s}^{-1}$  and a semiminor axis of  $0.04 \text{ m s}^{-1}$ . The aspect ratio of the ellipse implies that we may approximate the tide as unidirectional.

Observations of waves, surface currents, and water levels contextualize the modulations in the wave spectra. We observe significant wave height and peak frequency increasing on the following current and decreasing on the opposing current. Modulations occur near the swell peak of the spectra. Variations observed in the bulk parameters range from 10% to 30% (Table 2).

Directional spectra are estimated using MEM from the first four spectral moments recorded by the wave buoy. Figure 3 shows an example of directional spectra observed during a peak following current and then 6 h later at the subsequent peak opposing current. Consistent with the variations in the bulk parameters, we observe that the peak of the spectra is at

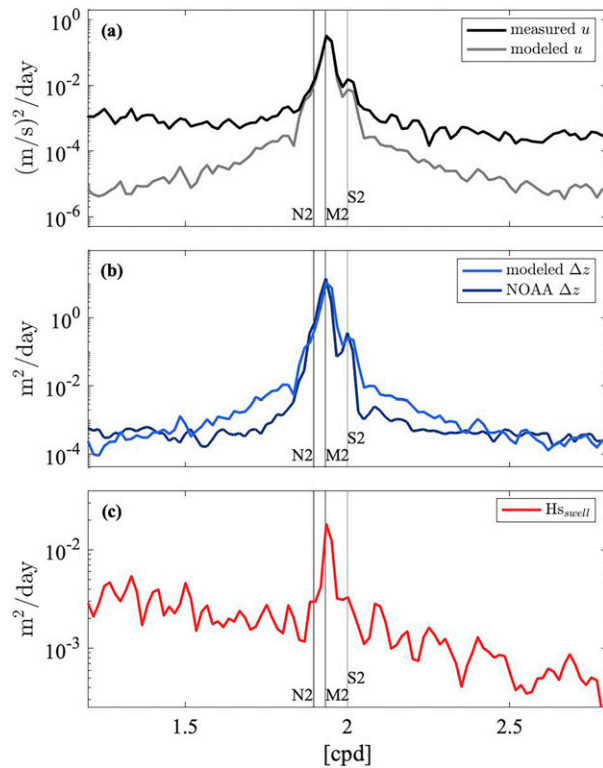


FIG. 2. Spectral analysis of (a) observed and modeled surface currents, (b) observed and modeled water levels, and (c) observed swell significant wave height  $H_{s,swell}$ . Vertical lines highlight dominant tidal constituents defined in Table 1. Note the high energy in the semidiurnal bands, particularly at the M2 frequency.

a higher frequency in the following current, and the spectra has higher energy overall. In addition, a slight focusing is observed. This is manifested in a shift of the peak period toward the direction of the following current. We also observe an overall narrowing or focusing of the spectra, corresponding to a shift in the direction spreading of around  $7^\circ$ .

### 3. Simplified theories for wave–tide interaction

Solutions for the change in wavenumber and frequency are found for two theories that treat the tide as a propagating shallow-water wave. The tidal wave generates the change in mean water depth and currents experienced by the surface

TABLE 2. Change in swell significant wave height  $\Delta H_{s,swell}$ , change in swell peak period  $\Delta T_{p,swell}$ , and change in swell directional spread  $\Delta \sigma_{swell}$  at the Fernandina Beach station CDIP132 from 1 Aug 2020 to 1 Aug 2021. Shown are the median and the 95th percentile of the percent change in the wave parameters.

	Median	95th percentile
$\Delta H_{s,swell}$	12%	25%
$\Delta T_{p,swell}$	11%	28%
$\Delta \sigma_{swell}$	9%	22%

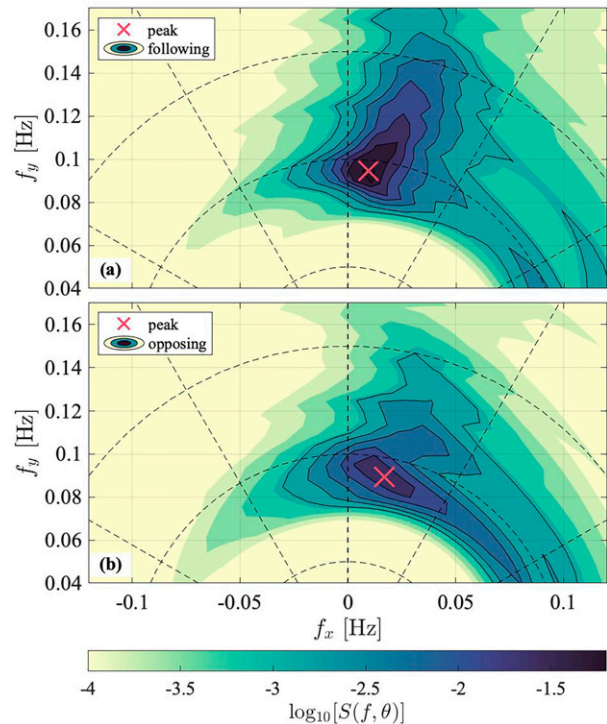


FIG. 3. Estimated directional spectra observed during (a) following currents ( $U = 0.32 \text{ m s}^{-1}$ ) and (b) opposing currents ( $U = -0.25 \text{ m s}^{-1}$ ) on 2130 18 Aug 2020— and 0330 19 Aug 2020—, respectively. Spectra are reoriented so that  $0^\circ$  points in the direction of the current ellipse (along  $x$  axis in Fig. 1a). In this example, the wave spectra were rotated to be aligned with the current ellipse along  $135^\circ$ . The red cross marks the peak of the spectra. The spectrum in following currents is more energetic, narrower, and shifted to higher frequencies than the spectrum in opposing currents.

gravity waves. The unsteadiness of the tide leads to results that may differ significantly from those formulated based on the condition that the currents, or changes in water depth, only vary in either space or time. Supplementing traditional wave modeling (e.g., Tolman 1990), we draw on the field of internal-wave and surface wave interaction (e.g., Gargett and Hughes 1972; Lenain and Pizzo 2021) and long wave–short wave interaction (e.g., Longuet-Higgins and Stewart 1960), to develop simplified models of wave–tide interaction.

Sections 3a and 3b describe these methods. The first theory uses solutions to geometrical optics and wave-action conservation with modulations driven by tidally varying currents and depth changes. The second theory, which is analytically and numerically simpler, is based on long wave–short wave interactions in a reference frame moving with the tide. Both cases consider irrotational, inviscid water waves in finite depth on a spatially and temporally evolving current and depth. The current and depth changes are related to each other, as they are taken to be tidally driven, and here we approximate the tide as a monochromatic shallow-water wave. Additionally, we assume that the incoming waves have constant action over the duration of consideration. That is, although the tides vary in time, we assume that the wave action is statistically steady. The goal is to

model the evolution of the wave spectrum given an initial spectral distribution, tidal current, and tidal amplitude.

*a. Governing equations*

Consider unidirectional linear surface gravity waves with vector wavenumber  $\mathbf{k}$ , absolute frequency  $\omega$ , energy  $E$ , and direction  $\theta$  relative to the  $x$  axis. These parameters are assumed to be slowly varying in space and time relative to the scales of the waves themselves. Following Mei et al. (2005), for a periodic plane wave solution with surface height  $\eta = ae^{i\Theta} + \text{c.c.}$  (where c.c. means complex conjugate) and amplitude  $a$  and phase  $\Theta(x, y, t) = \mathbf{k} \cdot \mathbf{x} - \omega t$ , the absolute frequency  $\omega$  and wavenumber  $\mathbf{k} = (k, \ell)$  for  $\mathbf{x} = (x, y)$  are related to the phase by

$$\omega = -\frac{\partial \Theta}{\partial t} \quad \text{and} \quad \mathbf{k} = \nabla \Theta. \tag{1}$$

When combined, these equations yield the conservation of wave crests equation

$$\frac{\partial \mathbf{k}}{\partial t} + \nabla \omega = \mathbf{0}. \tag{2}$$

The group velocity of wave energy is defined as

$$\mathbf{c}_g = \frac{\partial \sigma}{\partial \mathbf{k}}. \tag{3}$$

For waves on a weak current, the dispersion relation is modified to account for the change in background current velocity  $\mathbf{U} = (U, V)$ . The propagation velocity of the wave energy is then

$$\mathbf{c}_w = \mathbf{c}_g + \mathbf{U}, \tag{4}$$

and the absolute (or total) frequency as observed by a stationary observer is

$$\omega = \sigma + \mathbf{k} \cdot \mathbf{U}, \tag{5}$$

where  $\sigma$ , the relative (or intrinsic) frequency, follows the dispersion relation for surface gravity waves,

$$\sigma = \sqrt{g|\mathbf{k}| \tanh(|\mathbf{k}|h)}, \tag{6}$$

where  $g$  is the acceleration due to gravity,  $h$  is the water depth, and  $|\mathbf{k}| = \sqrt{k^2 + \ell^2}$ . The relative frequency  $\sigma$  is defined explicitly as a function of  $\mathbf{k}(\mathbf{x}, t)$  and  $h(\mathbf{x}, t)$ , so we can substitute Eq. (5) into Eq. (2) and expand each derivative to get the full equations for the change in wave parameters following Bretherton and Garrett (1968),

$$\frac{\partial \mathbf{k}}{\partial t} + (\mathbf{c}_g + \mathbf{U}) \cdot \nabla \mathbf{k} = -\frac{\partial \sigma}{\partial h} \frac{\partial h}{\partial \mathbf{x}} - \mathbf{k} \cdot \frac{\partial \mathbf{U}}{\partial \mathbf{x}} \quad \text{and} \tag{7}$$

$$\frac{\partial \omega}{\partial t} + (\mathbf{c}_g + \mathbf{U}) \cdot \nabla \omega = \frac{\partial \sigma}{\partial h} \frac{\partial h}{\partial t} + \mathbf{k} \cdot \frac{\partial \mathbf{U}}{\partial t}. \tag{8}$$

Wave energy propagation is governed by the conservation of wave action. Wave action is defined as the ratio between

wave energy and the intrinsic frequency  $A = E/\sigma$ . The wave-action conservation equation is

$$\frac{\partial A}{\partial t} + \nabla \cdot [(\mathbf{U} + \mathbf{c}_g)A] = S. \tag{9}$$

Here  $S$  represents the source terms in the wave-action balance, typically equal to  $S = S_{\text{in}} + S_{\text{diss}} + S_{\text{nl}}$ , the sum of the wind input, dissipation, and nonlinear wave-wave interactions, respectively. We set  $S = 0$  to examine only the dynamics of wave propagation under currents and depth variations independent of any forcing.

*b. 1D numerical solutions for waves propagating on a tide: Tolman's model*

To gain intuition for our system, we start by examining one-dimensional solutions to the equations of geometrical optics and conservation of wave action under the assumption of a one-dimensional tide. In one dimension, with  $x$  aligned with  $k$ , Eqs. (7)–(9) reduce to

$$\frac{\partial k}{\partial t} + (c_g + U) \frac{\partial k}{\partial x} = -\frac{\partial \sigma}{\partial h} \frac{\partial h}{\partial x} - k \frac{\partial U}{\partial x}, \tag{10}$$

$$\frac{\partial \omega}{\partial t} + (c_g + U) \frac{\partial \omega}{\partial x} = \frac{\partial \sigma}{\partial h} \frac{\partial h}{\partial t} + k \frac{\partial U}{\partial t}, \tag{11}$$

and

$$\frac{\partial A}{\partial t} + \frac{\partial}{\partial x} [(U + c_g)A] = 0, \tag{12}$$

where  $c_g$  and  $U$  are the group velocity and current in the  $\hat{x}$  direction. The group velocity is given by

$$c_g = \frac{\partial \sigma}{\partial k} = \frac{\partial}{\partial k} \left[ \sqrt{gk \tanh(kh)} \right], \tag{13}$$

and the propagation velocity of the wave energy along the axis  $x$  is given by

$$c_w = c_g + U. \tag{14}$$

Following the approach of Tolman (1990) and Vincent (1979), we seek periodic solutions for the advection of surface gravity waves by the tidal wave. We consider the tide to be a one-dimensional monochromatic progressive shallow-water wave of constant frequency  $\Phi$  and wavenumber  $K$ , with corresponding currents  $U$  and depth variations  $h$  as a function of the tidal phase  $\chi$  defined as

$$U(x, t) = A_u \sin[\chi(x, t)], \tag{15}$$

$$h(x, t) = \bar{h} + A_h \sin[\chi(x, t) + \varphi], \tag{16}$$

and

$$\chi(x, t) = Kx - \Phi t, \tag{17}$$

where  $A_u$  and  $A_h$  are the current and depth amplitude, respectively, and  $\bar{h}$  is the mean water depth. The term  $\varphi$  allows for a phase shift between water-level variation and currents as observed in many coastal tidal environments with mixed progressive and standing wave tides (Pugh 1987). The tidal propagation velocity is defined as the phase speed for shallow-water waves,

$$c_t = \Phi/K = \sqrt{gh}. \tag{18}$$

The shallow-water approximation holds for the tide so long as the tidal wavelength is much greater than the water depth, as is the case at Fernandina Beach in 16 m average water depth. We rewrite the governing Eqs. (10)–(12) as functions of  $\chi$ . The coordinates  $(x, t)$  must be changed to the tidal phase  $\chi = Kx - \Phi t$ , where the derivatives become

$$\begin{cases} \frac{\partial}{\partial x} = \frac{\partial}{\partial \chi} \frac{\partial \chi}{\partial x} = K \frac{\partial}{\partial \chi} \\ \frac{\partial}{\partial t} = \frac{\partial}{\partial \chi} \frac{\partial \chi}{\partial t} = -\Phi \frac{\partial}{\partial \chi} \end{cases} \tag{19}$$

We can now rewrite Eqs. (10)–(12) in terms of  $\chi$  to arrive at final expressions for the rate of change of wave parameters:

$$\frac{\partial k}{\partial \chi} = \frac{1}{c_t - (c_g + U)} \left[ \frac{\partial \sigma}{\partial h} A_h \cos(\chi + \varphi) + k A_u \cos \chi \right], \tag{20}$$

$$\frac{\partial \omega}{\partial \chi} = \frac{c_t}{c_t - (c_g + U)} \left[ \frac{\partial \sigma}{\partial h} A_h \cos(\chi + \varphi) + k A_u \cos \chi \right], \tag{21}$$

and

$$\frac{\partial A}{\partial \chi} = A \frac{1}{c_t - (c_g + U)} \left( \frac{\partial c_g}{\partial \chi} + A_u \cos \chi \right). \tag{22}$$

From these equations, we identify the generalized behavior of the modulations in wavenumber, frequency, and wave action. The common term in the denominators, which we will call  $c_*$ ,

$$c_* = c_t - (c_g + U), \tag{23}$$

determines the magnitude and sign of the modulations set by Eqs. (20)–(22). In particular, when  $|c_*|$  is small, the modulations to the surface waves are large. This occurs when the tidal wave and the surface waves have similar speeds,  $c_t \approx c_g + U = |c_w|$ . For the progressive shallow-water tide, modulations in surface wave parameters are most amplified at low frequencies because their propagation velocities  $c_w$  approach the tide’s shallow-water phase (and group) speed  $\sqrt{gh}$ . The  $c_*$  term in the denominator of each equation can also change sign if  $c_t$  is either larger or smaller than the wave-action propagation velocity.

To compare the relative contributions due to depth variations or currents, we can compare the coefficients in front of each phase-dependent term associated with changes in depth

or changes in currents in Eqs. (20) and (21). When the nondimensional term

$$\gamma = \frac{k A_u}{\frac{\partial \sigma}{\partial h} A_h} \tag{24}$$

is greater than or less than 1, currents or depth changes, respectively, dominate the modulation in wavenumber. The phase difference due to  $\varphi$  in Eqs. (20) and (21) can also alter the relative influence of depths and currents as well as the total magnitude of modulations. For example, current and depth variations are out of phase ( $\varphi = \pi$ ); then, when  $\gamma \approx 1$ , the depth modulations and current modulations can effectively cancel out. When  $\varphi = 0$ , the two contributions to wave modulations will constructively add. However, other values of  $\varphi$  can lead to peaks in wavenumber or wave energy modulation that are not in phase with either the depth variations or the currents. Typical values for  $c_*$  and  $\gamma$  will be evaluated at Fernandina Beach in section 3d.

In summary, we identify a phase space that governs the variations in wave parameters due to tides. This space includes not just the magnitude of currents and depth variations,  $A_u$  and  $A_h$ , but also wavenumber  $k$ , energy  $E$ , mean depth  $\bar{h}$ , phase  $\varphi$ , and tide phase speed  $c_t$ . Full solutions can be found to this system of equations by solving them numerically using an explicit Runge–Kutta method with variable time steps given initial conditions  $k_0 = k(\chi = 0)$ ,  $\omega_0 = \omega(\chi = 0)$ ,  $A_0 = A(\chi = 0)$  (Shampine and Reichelt 1997). This approach allows us to derive simplified governing equations for surface wave modulation due to tidally driven currents and depth variations, further quantifying the importance of different forcing parameters, including current magnitude, water depth, and tide phase speed. However, this approach is limited by its computational complexity, which, while relatively simple, becomes apparent when generalizing the system to two dimensions. The next section presents an alternative approach that allows us to model two-dimensional effects with less computational complexity. We adopt a convenient perspective often applied to understanding the interaction between internal waves and surface waves by working in a reference frame moving with the tide (Longuet-Higgins and Stewart 1960). This method is described in the next section.

*c. Long wave–short wave solutions for tides and surface gravity waves*

In the fixed reference frame of the buoy, absolute frequency is not conserved as currents  $U$  and water depth  $h$  vary with time. However, following Phillips (1966), we can work in a frame of reference moving with the tidal wave at phase speed  $c_t$ . As  $U$  and  $h$  only vary with the phase of the tide, the absolute frequency in this reference frame has no explicit dependence on time,

$$\frac{d\omega_t}{dt} = 0. \tag{25}$$

The absolute frequency in this frame of reference  $\omega_t$  is modified from Eq. (5) for the fixed frame and is given by

$$\omega_t = \sigma + \mathbf{k} \cdot (\mathbf{U} - \mathbf{c}_t). \tag{26}$$

The conservation of absolute frequency [Eq. (25)] then implies that

$$\sigma_0 + |\mathbf{k}_0|(-c_t) \cos \theta_0 = \sigma + |\mathbf{k}|(U - c_t) \cos \theta. \tag{27}$$

Subscript 0 denotes an initial condition where tidal currents are negligible. The angle  $\theta$  is the angle between the waves and the  $x$  axis, which we choose to be aligned with the current. The refraction of the waves is determined by the fact that the wavenumber is the gradient of a scalar (i.e., the phase), so that its curl is zero. This result, known as Snell’s law, implies that in the absence of transverse currents, we have

$$|\mathbf{k}_0| \sin \theta_0 = |\mathbf{k}| \sin \theta. \tag{28}$$

With some manipulation, Snell’s law tells us that if the magnitude of the wavenumber varies, so too will variations in  $\theta$ . We can illustrate this from Eq. (28) with a few assumptions: ignoring the variation in the horizontal component, we make a small perturbation expansion for variations in  $k$  and  $\theta$ , where  $k \approx k_0 + \Delta k$  and  $\theta \approx \theta_0 + \Delta \theta$ . Then by small-angle and first-order approximation, Eq. (28) becomes

$$\frac{\Delta k}{k_0} \approx -\frac{\Delta \theta}{\tan \theta_0}. \tag{29}$$

In the one-dimensional approximation, we assume that the waves and currents are aligned and there is no refraction. We are able to find solutions for the modulated wavenumber  $|\mathbf{k}|$  to Eq. (27) through the relation

$$\begin{aligned} \sqrt{g|\mathbf{k}_0| \tanh(|\mathbf{k}_0|h_0)} + |\mathbf{k}_0|(-c_t) &= \sqrt{g|\mathbf{k}| \tanh(|\mathbf{k}|h)} \\ &+ |\mathbf{k}|(U - c_t). \end{aligned} \tag{30}$$

In two dimensions, we find  $\theta$  by substituting  $|\mathbf{k}| = |\mathbf{k}_0| \sin \theta_0 / \sin \theta$  into Eq. (27) and solving the following equation for  $\theta$ :

$$\begin{aligned} \sigma_0 - |\mathbf{k}_0|c_t \cos \theta_0 &= \sqrt{g|\mathbf{k}_0| \frac{\sin \theta_0}{\sin \theta} \tanh\left(|\mathbf{k}_0| \frac{\sin \theta_0}{\sin \theta} h\right)} \\ &+ |\mathbf{k}_0| \frac{\sin \theta_0}{\sin \theta} (U - c_t) \cos \theta. \end{aligned} \tag{31}$$

The wavenumber is then found by solving Eq. (27) for  $|\mathbf{k}|$ . Solutions for both  $\theta$  and  $|\mathbf{k}|$  are found numerically using the Newton–Raphson method.

The wave-action equation for a single wavenumber given in Eq. (9) is extended to include a full spectrum of surface waves with a variable wavenumber  $k = k_x$  in the direction of the current  $x$  (e.g., Fig. 1a) and constant in the off-axis  $y$ ,  $\ell = \ell_0 = k_y$ , following Hughes (1978) for  $Adkd\ell_0$  over a narrow band of  $k, \ell$  space,

$$\frac{\partial A}{\partial t} + (c_g + U) \frac{\partial A}{\partial x} = 0. \tag{32}$$

In the tide reference frame where wave parameters are time independent, we find that

$$\begin{aligned} A(k, \ell_0)dkd\ell_0 &= A_0(k_0, \ell_0)dkd\ell_0 \\ &= A_0(k_0, \ell_0) \frac{\partial k}{\partial k_0} dk_0 d\ell_0. \end{aligned} \tag{33}$$

The behavior of the Jacobian  $\partial k / \partial k_0$  is found following Hughes (1978). We differentiate Eq. (2) with respect to  $k_0$  in the reference frame moving with the tidal wave, using the definition for  $\omega$  as  $\omega_t$  in Eq. (26), to find the Jacobian

$$(c_g + U - c_t) \frac{\partial k}{\partial k_0} = c_{g,0} - c_t. \tag{34}$$

In summary, the shifted energy is calculated as

$$E(k, \ell_0)dkd\ell_0 = E_0(k_0, \ell_0) \frac{\sigma}{\sigma_0} \frac{c_{g,0} - c_t}{(c_g + U - c_t)} dk_0 d\ell_0. \tag{35}$$

The above expression relates an initial vector-wavenumber spectrum to the final vector-wavenumber spectrum modulated by a tidal wave with phase speed  $c_t$  and induced current  $U$ . The final step is to relate the vector-wavenumber spectrum  $E(k, \ell)$  to the observed absolute frequency spectrum  $E(\omega, \theta)$  measured by a moored, stationary wave buoy. This step is detailed in the appendix.

In summary, this approach allows us to reduce this problem to a series of simple algebraic equations that are easily solved and replicate the numerical model for solutions to the coupled ODEs in the previous section. See also the related discussion in Gargett and Hughes (1972) and Lenain and Pizzo (2021). The next section uses the two approaches to model the theoretical response of a wave spectra to tidal currents and depths for the Fernandina Beach environment.

#### d. Model predictions

The two simplified models lead to equivalent results, and each has advantages in modeling and interpreting wave–tide interaction. To gain intuition about the predictions of the models, we force them with conditions that replicate the Fernandina Beach environment ( $A_u = 0.25 \text{ m s}^{-1}$ ,  $A_h = 1 \text{ m}$ , and  $\bar{h} = 16 \text{ m}$ ). We illustrate in Fig. 4 the response of a one-dimensional JONSWAP wave spectrum under the influence of currents and depth variations induced by tides as found by solutions to Eqs. (31), (27), and (35) in one dimension; that is,  $\theta = 0$ . The simulated spectrum has a peak at 10 s. We show two cases, one in which the phase speed of the tide is zero,  $c_t = 0$  (Fig. 4a), and one in which the phase speed of the tide is the shallow-water phase speed,  $c_t = \sqrt{g\bar{h}}$  (Fig. 4b). In the first case, we see that a following current shifts the spectra to lower energy and an opposing current shifts the spectra to higher energy. However, when  $c_t = \sqrt{g\bar{h}}$ , the model predicts variations more similar to those observed at Fernandina Beach. A following current will shift the spectra to higher energy and frequency, and vice versa for the opposing case. The relationship with a change

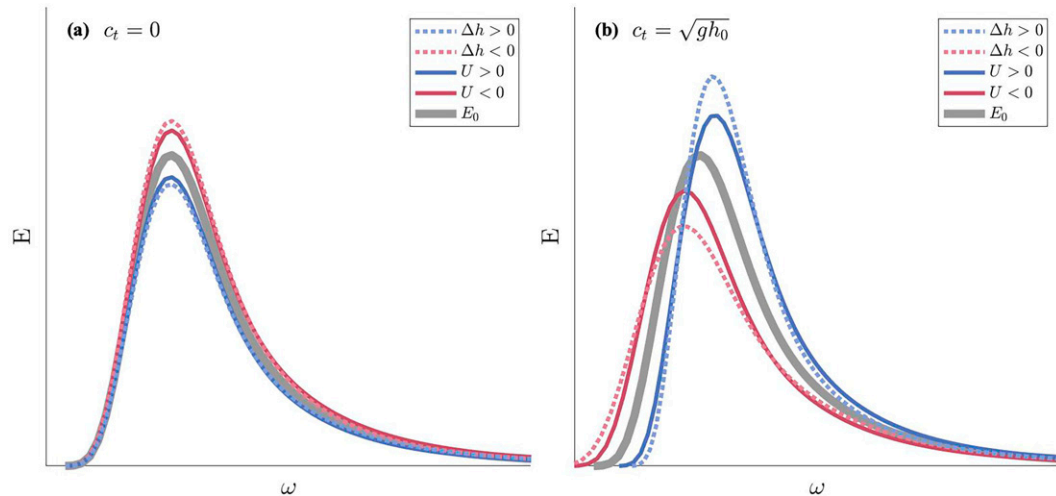


FIG. 4. Given an incident wave spectrum (gray), we show the resulting shift due to a change in current (solid) or a change in water level (dashed) as predicted by the model given by Eqs. (31), (27), and (35). We show the shift corresponding to a following and opposing current (blue and red solid lines, respectively) and an increase or decrease in water level (blue and red dashed lines, respectively) for the two separate circumstances in which the tidal propagation velocity parameter  $c_t$  is equal to (b) the shallow water wave phase speed or (a) zero. Note the change in sign of the spectral deviations from (a) to (b) in response to the same forcing.

in water depth is similar, where an increase in water-level shifts the spectra lower when  $c_t = 0$  and higher when  $c_t = \sqrt{g\bar{h}}$ .

Tolman's model highlights the importance of the sign of  $c_t - (c_g + A_u)$  in modulating the maxima and minima of the significant wave height and peak period. The terms in Eqs. (23) and (24) from the model analysis in section 3b allow us to identify the size and sign of variations expected at Fernandina Beach and interpret the modeled spectra in Fig. 4. As before, we use variables that replicate conditions at Fernandina Beach ( $A_u = 0.25 \text{ m s}^{-1}$ ,  $A_h = 1 \text{ m}$ , and  $\bar{h} = 16 \text{ m}$ ). The group velocity  $c_g$  is found by estimating the wavenumber for a 10-s peak period using the dispersion relation in Eq. (6). We also assume that the tide acts as a progressive shallow-water wave,  $c_t = \sqrt{g\bar{h}}$ . Under these conditions,  $c_* = 3.27$ . The positive value of  $c_*$  indicates that the wavenumber variations will be in phase with the oscillation of currents or depth, that is, as currents increase and become positive, the change in wavenumber will increase. Similarly, as currents decrease and become negative, the change in wavenumber will decrease. In comparison, when  $c_t = 0$  for these exact same conditions,  $c_*$  is negative and much larger in magnitude, with  $c_* = -9.25$ . The change in the sign of  $c_*$  is consistent with the difference between the simulated spectra in Fig. 4, where the responses between the two conditions are of opposite sign.

The smaller magnitude of  $c_*$  when  $c_t = \sqrt{g\bar{h}}$  also indicates that the modulation in the surface waves will be large, which is clear in Fig. 4 as the shift in the wave spectra is nearly 3 times as large as for the case in which  $c_t = 0$ . From this analysis, we also conclude that currents and water-depth modulations are approximately balanced at the 10-s peak, with current changes slightly dominating the modulation, as  $\gamma \approx 1.17$ . In comparison, for slightly lower frequencies at 12 s, depth variations dominate the modulation as  $\gamma \approx 0.96$ , and, for slightly higher

frequencies at 8 s, current variations dominate the modulation as  $\gamma = 1.76$ .

The model developed using a long wave–short wave approximation described in section 3c allows us to gain intuition behind the individual physical mechanisms at play with minimal computational complexity. The case of internal wave–surface wave interaction, when the phase speed of the internal wave is typically less than that of the surface waves, can be represented by the example with  $c_t \ll 1$ . With tides, the phase speed  $c_t = \sqrt{g\bar{h}}$  is typically larger than that of the surface waves, which is why in wave–tide interactions, the response of the surface waves to currents can be opposite.

The key to interpreting the change in sign of the modulations is noting the different speeds of the long wave in question. Most surface waves—including long-period swell—propagate slower than the phase speed of the tide, which here we take to be a shallow-water wave. In the reference frame moving with the long wave, the slower surface waves now appear to propagate backward. In this reference frame, what was previously surface waves propagating in the same direction as the current, now the surface waves oppose the direction of the current. The frequency and steepness thus increase. Returning to the fixed frame, this shift is maintained, yet the definition of following/opposing current switches again, and we observe surface waves steepening on following currents.

If the tides and waves are not aligned, the apparent tide phase speed is smaller than the shallow-water phase velocity by a factor that is the cosine of the angle between the waves and the tide, and the response of the surface waves can differ and be more complicated. This might explain why the literature contains observations with various phases between the maximum wave amplitudes and the maximum tidally induced currents (e.g., Barber 1949; Tolman 1988; Masson

1996; Davidson et al. 2008; Gemmrich and Garrett 2012; Guillou 2017; Wang and Sheng 2018).

The two-dimensional model that simulates directional frequency spectra implies that not only does the frequency and energy increase on the following current, there is also directional focusing toward the direction of tidal wave propagation, similar to that observed at Fernandina Beach. Conversely, an opposing current increases directional spreading for a given incident wave away from the direction of the long-wave propagation. This can impact both the directional spread and the location of the peak of the directional spectrum in the cases where the peak is off axis of the current vector.

Simulations of modeled spectra also show the sensitivity to the value of  $c_t$  when  $c_t$  approaches  $c_w$ , as described in section 3b. The methods fail when there are no solutions to Eq. (27), which occurs when the short-wave propagation velocity nears the tidal phase speed, i.e.,  $c_t = c_w = c_g + U$ , such that waves cannot travel upstream. Classically, this is known as the blocking frequency (Phillips 1966; Gargett and Hughes 1972). In the ocean, a combination of breaking and reflection likely occur (Chawla and Kirby 2002; Ardhuin et al. 2010, 2012), but these effects are not incorporated into this simplified model. In general,  $c_t$  becomes an important parameter to describe the sign of the wave modulations with respect to the currents. Even when  $c_t$  does not equal  $c_w$ , small variations in the value of  $c_t$  can alter the magnitude of variation in the surface waves.

#### 4. Comparison with observations

We use the methods developed in section 3 to model the tidal variations observed in the wave measurements from the Fernandina Beach CDIP station. Equations (27) and (31) are solved algebraically to estimate the change in wavenumbers and then used in Eq. (35) to find the modulated directional spectrum  $E(k, \ell)$ . The initial condition  $E_0(k_0, \ell_0)$  is taken from the observed directional absolute frequency spectrum  $E_0(\omega_0, \theta_0)$  when the current magnitude is zero to represent an “unmodulated” spectrum. The observed directional spectra are averaged over 90 min to reduce noise. The initial condition is converted to vector wavenumber spectra, and the result from the model is converted back to absolute frequency spectra via Eq. (A3). Because the mid-Atlantic Bight and study region are dominated by semidiurnal tides (Table 1), we are able to approximate the tide with a single constituent. We use periodic M2 tidal fits to the observed water depth and surface currents to force the simulation. This model can be run at any time step with any frequency resolution, so we chose to simulate the modulated spectra at the same intervals of the observations to facilitate the comparison. However, higher resolutions are easily achieved with minimal added computational costs.

We present a comparison of the modeled wave spectra over 1 day beginning at 0900 UTC 20 August 2020 in Figs. 5 and 6. Time is expressed as a function of the tidal phase  $\chi$ , where  $2\pi$  covers 12.42 h. This subsection of the observations was chosen for this example because the incident swell was relatively constant during this time period, isolating the impact of the

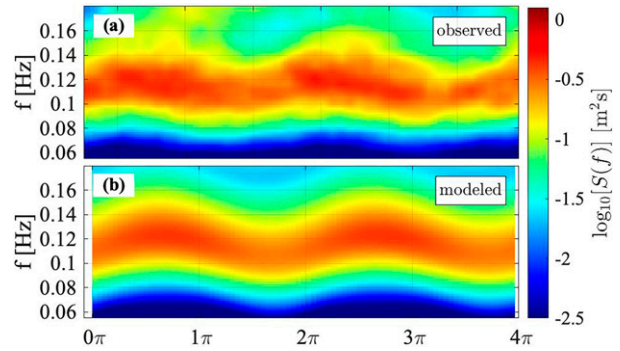


FIG. 5. Wave spectrogram observed over (a) 1 day, and (b) reproduced wave spectrogram from the numerical model of the omnidirectional spectra developed using observations to set the initial condition and forcing terms (currents and depth variations). The modeled spectrogram mimics the increase and decrease in frequency of the observed swell band. The model tends to overestimate the variation in lower frequencies.

tidal variations. We discuss the implications of a varying background wave field later in this section.

The model captures the variations in the wave spectra and the bulk parameters due to the tides. The omnidirectional spectrum shown in Fig. 5 is calculated from the modeled directional spectrum by integrating over all directions. The modeled energetic swell band in Fig. 5 is shifted upward and amplified at  $\pi/2$  and is shifted downward later at  $3\pi/2$ , similar to the observed spectrogram. The one-dimensional spectra at the minima and maxima of the current variations are shown in Fig. 6a. Both the modeled and observed spectra shift downward in energy and frequency during the opposing current and shift higher during the following current. The observed peak shifted from 0.119 Hz ( $0.409 \text{ m}^2 \text{ s}^{-1}$ ) to 0.109 Hz ( $0.271 \text{ m}^2 \text{ s}^{-1}$ ), and the modeled peaks shifted from 0.121 Hz ( $0.404 \text{ m}^2 \text{ s}^{-1}$ ) to 0.107 Hz ( $0.294 \text{ m}^2 \text{ s}^{-1}$ ). Potential causes for the overestimation of modulation at lower frequencies, also visible in Fig. 5, are discussed in section 5.

Model deviations from the observed spectra can also occur when nonlocal or wind-driven energy influences the wave spectra. We chose to model  $f < 0.2$  Hz in part because this band of the surface wave spectrum is most strongly modulated by the tides and to avoid the shorter time-scale variability in wind forcing as seen around  $1\pi$  in Fig. 5. Here the observed high-frequency waves ( $f > 0.1$  Hz) become more energetic due to changing wind conditions that are not accounted for in this wave–tide numerical model that does not include source/sink terms. Likewise, a decrease in significant wave height over  $2\pi$  in Fig. 6 is unaccounted for as the presented tidal model does not account for dispersion or decrease in energy from long-period remote swell. When we do not update the background energy after initiating the model, the model begins to decorrelate from the observations after about  $4\pi$  (about 1 day), which is the approximate time scale of variations for wind events and modulations in direction and magnitude of the remotely forced swell.

Figure 6 shows the change in significant wave height and peak period at Fernandina Beach and how the model predicts

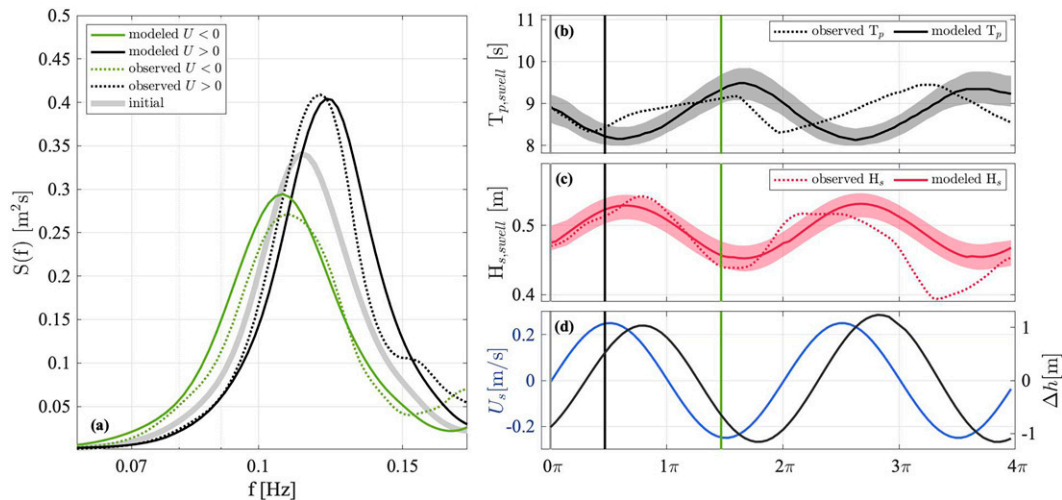


FIG. 6. Observations are used as an initial condition to estimate (d) the resulting shift of the directional spectrum under tidal currents (blue) and water-level variations (black). (a) The omnidirectional spectrum resulting from following current (black) and opposing current (green) for both the observations and the model. The initial condition for this run is shown in gray. Also shown are the bulk parameters ( $0.05 < f < 0.18$  Hz) for both the model and observations including (b) peak frequency and (c) significant wave height. The shaded region corresponds to varying the magnitude of the maximum current speed and depth changes by up to 50%.

similar variations in bulk parameters when current and depth conditions match observations. The shaded region indicates variations due to errors up to 50% of the total current or depth variation magnitudes. From a following to opposing current, the model significant wave height varies from 0.52 to 0.46 m (12% decrease), and the observed significant wave height varies from 0.51 to 0.44 m (13% decrease). This model peak period varies from 8.2 to 9.3 s (13% increase) and the observed peak period varies from 8.4 to 9.1 s (9% increase). The timing of the minima and maxima of the bulk parameters shown are not coincident with the minima and maxima of the surface currents, indicating the modulations due to water level contribute to the change in bulk parameters, as estimated by  $\gamma$ . We still predict that the following current coincides with an increase in significant wave height and decrease in peak period, as observed in the measurements. There is a lag in the modeled peak period with respect to the observations, which can be associated with the overestimation of low frequencies or unresolved physical processes, discussed in section 5. Nevertheless, the bulk-scale agreement between the relatively simple model and the observations is encouraging. For this time range, the model predicts a percent change equivalent to that observed and within observed median values for the observations at CDIPI32 (Table 2).

Directional effects are also modeled and compared with observations of directional spectra, which indicate that a slight focusing and a shift in peak direction occur. Observations of shifts in the mean directional spread in the swell band of up to  $10^\circ$  (e.g., Fig. 3) are modeled in the directional spectrum.

In general for the environment at Fernandina Beach, with variations in water levels up to 1 m and tidal currents up to  $0.2 \text{ m s}^{-1}$ , the model predicts variations of significant wave height of up to 25%. This agrees with average values variations

in observed significant wave height from Table 2, even with the simple assumption of a uniform incident wave spectrum and simple shallow-water tidal wave propagation. Overall, the model confirms that tides will induce changes in the wave field that will manifest in both lower- and higher-order moments.

## 5. Discussion

Further work to investigate the impact of wave–tide interaction on wave breaking and dissipation using third-generation models could be beneficial to understanding the impact of this phenomena in the broader wave and Earth system. This includes addressing issues in this simplified model when the speed of long wave  $c_l$  nears the propagation velocity of surface waves  $c_w$  and blocking occurs. This is manifested as a critical point in the variables and subsequently the model breaks down. Expanding this work to other locations will help assess any variability in the surface wave modulation by tides related to the wave climatology and various tidal conditions. This work highlights the need for measurements of surface currents and directional wave spectra at other locations with different tidal environments. For example, the model is limited to only using a single tidal phase  $\chi$  or constituent, which may cause issues when applying this in regions with mixed semidiurnal and diurnal tides. For regions with mixed tides, the reference frame will need to be chosen carefully for the method that relies on working in a reference frame where there are no explicit temporal variations. We have also assumed that the tide is a shallow-water progressive wave, and further work should be done to characterize the variability of the phenomena under mixed standing and progressive wave tides, amplified tides, and other coastal wave complexity. This may change the formulation of  $c_l$ . Further work can incorporate

observations of tidal variation in wave energy at other locations to assess variation with different tidal environments.

This work reiterates the importance of careful interpretation of the reference frame of our observations. It is clear that the reference frame of the observer plays an important role, as noted by work on interpreting wave measurements from propelled platforms like ships and wave gliders and from remote sensing via satellite and HF radar (Longuet-Higgins 1986; Ardhuin et al. 2009; Collins et al. 2017). To integrate and compare multiple varieties of observations and models, especially with the advent of current-measuring satellites such as *Surface Water and Ocean Topography (SWOT)*, it will be important to carefully consider the measurements.

### 6. Conclusions

In conclusion, this work presents theoretical and numerical models that help understand how tides can modulate surface waves. We present observations of significant tidal modulations in wave records from a moored buoy at Fernandina Beach, which shows strong modulations to the surface wave field in frequency, magnitude, and direction. Following tidal currents correspond with an increase in wave height of up to 25%, contrary to the canonical textbook example where waves steepen on opposing steady homogeneous currents. We describe the observed modulations through a simplified theoretical framework that models the tide as a progressive shallow-water wave, effectively treating the problem as a long wave–short wave interaction. By working in the reference frame moving with the tidal wave, we have simplified the problem from a system of partial differential equations to algebraic equations, which reduces the computational complexity significantly. The model shows that when the phase speed of long waves is faster than propagation velocity of surface waves, steepness can increase on following tidal currents. Key nondimensional parameters are identified that characterize the size of tidal modulations in wave parameters. Numerical solutions to this model reproduce the observed wave modulations due to tidal currents and changes in water depth at Fernandina Beach.

With the framework developed in this study, we characterize the size and sign of tidal modulations in wave parameters. Surface waves will be amplified by the tide when they propagate in the direction of the tidal currents and when the speed of the surface waves propagation nears the speed of the tidal wave. This will be dependent on wave frequency, water depth, and current magnitude. When the speed of the tidal wave exceeds the speed of the surface gravity wave propagation, tidal currents following the direction of surface wave propagation can lead to an increase in surface wave height and frequency. At Fernandina Beach, where the dominant wave direction is aligned with the tides, this leads to amplification of the peak of the spectrum.

This work has demonstrated the ability to understand significant tidal variations in wave spectra by treating the interaction between surface waves and the tide as a long wave–short wave interaction. This treatment allows us to understand how waves respond to tidally induced currents and depth variations, important for maritime safety and navigation, coastal management

and adaptation strategies, and accurate nearshore wave forecasts, proposing an explanation for the common surfing phenomena known as the tidal push, where incident wave heights increase during the rising tide. This highlights the importance of careful interpretation of measurements and models for both public and scientific application. Future numerical work will explore the impact of wave breaking, relative wind, and shorter time-scale variability in wave fields. This framework will also be used to constrain observed variation in surface waves due to tides and provide statistical estimates for wave variations due to tides at other nearshore environments.

*Acknowledgments.* The authors thank Bia Villas Bôas, Bill O’Reilly, Fabrice Ardhuin, Eric Terrill, and Mark Merrifield for numerous helpful discussions. This work benefited from close collaboration with members of the CDIP team, including Jim Behrens and Corey Olfe. Last, we are thankful to the two anonymous reviewers for their insightful feedback, which improved the paper. This work is funded by the U.S. Army Corps of Engineers through Cooperative Ecosystem Studies Unit (CESU) W912HZ 1920020.

*Data availability statement.* Wave data were furnished by the Coastal Data Information Program (CDIP) Integrative Oceanography Division, operated by the Scripps Institution of Oceanography, under the sponsorship of the U.S. Army Corps of Engineers and the California Department of Parks and Recreation. Water level data are from NOAA Tides and Currents. Bathymetry at Fernandina Beach is from the NOAA National Centers for Environmental Information (NOAA 2014). All data used in this paper are publicly available (<https://cdip.ucsd.edu>; <https://tidesandcurrents.noaa.gov>; [www.ncei.noaa.gov](http://www.ncei.noaa.gov)). Data and analysis are collected in Ho et al. (2022).

## APPENDIX

### Comparison with Observations

We express the output in the more-traditional absolute frequency spectrum  $E(\omega, \theta)$  to relate to the omnidirectional frequency spectrum measured by a moored, stationary wave buoy. This is calculated via the Jacobian transformation between frequency and wavenumber as

$$E(\omega, \theta)d\theta d\omega = E(\kappa, \ell)d\kappa d\ell = E(\kappa, \ell)\kappa d\kappa d\theta. \tag{A1}$$

This is rearranged for the final expression for the directional absolute frequency spectrum,

$$E(\omega, \theta) = \kappa \frac{\partial \kappa}{\partial \omega} E(\kappa, \ell) = \kappa(c_g + U)^{-1} E(\kappa, \ell). \tag{A2}$$

The derivative of absolute frequency with respect to  $\kappa$  was rewritten using the definition in Eq. (5) via

$$\frac{\partial \omega}{\partial \kappa} = \frac{\partial}{\partial \kappa} (\sigma + \kappa U) = c_g + U. \quad (\text{A3})$$

Last, the omnidirectional spectrum is found by integrating over all directions for a fixed frequency, which requires interpolation:

$$E(\omega) = \int_0^{2\pi} E(\omega, \theta) d\theta. \quad (\text{A4})$$

It is important to note that the Jacobian transformation from wavenumber space to spectra in terms of absolute frequency and direction is not well behaved, because there is a singularity at the blocking point (Tolman and Booij 1998). See also the discussion on the blocking point in section 5.

## REFERENCES

- Arduin, F., L. Marié, N. Rasclé, P. Forget, and A. Roland, 2009: Observation and estimation of Lagrangian, Stokes, and Eulerian currents induced by wind and waves at the sea surface. *J. Phys. Oceanogr.*, **39**, 2820–2838, <https://doi.org/10.1175/2009JPO4169.1>.
- , and Coauthors, 2010: Semiempirical dissipation source functions for ocean waves. Part I: Definition, calibration, and validation. *J. Phys. Oceanogr.*, **40**, 1917–1941, <https://doi.org/10.1175/2010JPO4324.1>.
- , and Coauthors, 2012: Numerical wave modeling in conditions with strong currents: Dissipation, refraction, and relative wind. *J. Phys. Oceanogr.*, **42**, 2101–2120, <https://doi.org/10.1175/JPO-D-11-0220.1>.
- , S. T. Gille, D. Menemenlis, C. B. Rocha, N. Rasclé, B. Chapron, J. Gula, and J. Molemaker, 2017: Small-scale open ocean currents have large effects on wind wave heights. *J. Geophys. Res. Oceans*, **122**, 4500–4517, <https://doi.org/10.1002/2016JC012413>.
- Barber, N. F., 1949: The behaviour of waves on tidal streams. *Proc. Roy. Soc. London*, **198A**, 81–93, <https://doi.org/10.1098/rspa.1949.0088>.
- Barnes, M. A., and C. Rautenbach, 2020: Toward operational wave-current interactions over the Agulhas Current system. *J. Geophys. Res. Oceans*, **125**, e2020JC016321, <https://doi.org/10.1029/2020JC016321>.
- Baschek, B., 2005: Wave-current interaction in tidal fronts. ‘Aha Huliko‘a Hawaiian Winter Workshop, Honolulu, HI, University of Hawai‘i at Mānoa, 131–138, <http://www.soest.hawaii.edu/PubServices/2005pdfs/Baschek.pdf>.
- Bôas, A. B., and Coauthors, 2019: Integrated observations of global surface winds, currents, and waves: Requirements and challenges for the next decade. *Front. Mar. Sci.*, **6**, 425, <https://doi.org/10.3389/fmars.2019.00425>.
- Booij, N., R. C. Ris, and L. H. Holthuijsen, 1999: A third-generation wave model for coastal regions: 1. Model description and validation. *J. Geophys. Res.*, **104**, 7649–7666, <https://doi.org/10.1029/98JC02622>.
- Bretherton, F. P., and C. J. R. Garrett, 1968: Wavetrains in inhomogeneous moving media. *Proc. Roy. Soc. London*, **302A**, 529–554, <https://doi.org/10.1098/rspa.1968.0034>.
- Bühler, O., and T. E. Jacobson, 2001: Wave-driven currents and vortex dynamics on barred beaches. *J. Fluid Mech.*, **449**, 313–339, <https://doi.org/10.1017/S0022112001006322>.
- , and M. E. McIntyre, 2005: Wave capture and wave–vortex duality. *J. Fluid Mech.*, **534**, 67–95, <https://doi.org/10.1017/S0022112005004374>.
- Cavaleri, L., and Coauthors, 2007: Wave modelling—The state of the art. *Prog. Oceanogr.*, **75**, 603–674, <https://doi.org/10.1016/j.pocean.2007.05.005>.
- Chawla, A., and J. T. Kirby, 2002: Monochromatic and random wave breaking at blocking points. *J. Geophys. Res.*, **107**, 3067, <https://doi.org/10.1029/2001JC001042>.
- Collins, C. O., III, and Coauthors, 2017: Doppler correction of wave frequency spectra measured by underway vessels. *J. Atmos. Oceanic Technol.*, **34**, 429–436, <https://doi.org/10.1175/JTECH-D-16-0138.1>.
- Datawell B. V., 2021: Datawell Waverider manual DWR4. Datawell B.V. Doc., 149 pp., [https://datawell.nl/wp-content/uploads/2022/09/datawell\\_manual\\_dwr4.pdf](https://datawell.nl/wp-content/uploads/2022/09/datawell_manual_dwr4.pdf).
- Davidson, M. A., T. J. O’Hare, and K. J. George, 2008: Tidal modulation of incident wave heights: Fact or fiction? *J. Coastal Res.*, **24**, 151–159, <https://doi.org/10.2112/06-0754.1>.
- Egbert, G. D., and S. Y. Erofeeva, 2002: Efficient inverse modeling of barotropic ocean tides. *J. Atmos. Oceanic Technol.*, **19**, 183–204, [https://doi.org/10.1175/1520-0426\(2002\)019<0183:EIMOBO>2.0.CO;2](https://doi.org/10.1175/1520-0426(2002)019<0183:EIMOBO>2.0.CO;2).
- Erofeeva, S., L. Padman, and S. L. Howard, 2020: TMD Matlab Toolbox, version 2.5. GitHub, accessed 4 April 2020, [https://github.com/EarthAndSpaceResearch/TMD\\_Matlab\\_Toolbox\\_v2.5](https://github.com/EarthAndSpaceResearch/TMD_Matlab_Toolbox_v2.5).
- Gargett, A. E., and B. A. Hughes, 1972: On the interaction of surface and internal waves. *J. Fluid Mech.*, **52**, 179–191, <https://doi.org/10.1017/S0022112072003027>.
- Gemmrich, J., and C. Garrett, 2012: The signature of inertial and tidal currents in offshore wave records. *J. Phys. Oceanogr.*, **42**, 1051–1056, <https://doi.org/10.1175/JPO-D-12-043.1>.
- Guillou, N., 2017: Modelling effects of tidal currents on waves at a tidal stream energy site. *Renewable Energy*, **114A**, 180–190, <https://doi.org/10.1016/j.renene.2016.12.031>.
- Hanson, J. L., B. A. Tracy, H. L. Tolman, and R. D. Scott, 2009: Pacific hindcast performance of three numerical wave models. *J. Atmos. Oceanic Technol.*, **26**, 1614–1633, <https://doi.org/10.1175/2009JTECHO650.1>.
- Ho, A., S. T. Merrifield, and N. Pizzo, 2022: Data from: Wave-tide interaction for a strongly modulated wave field. UC San Diego Library Digital Collections, <https://doi.org/10.6075/JOWD40R1>.
- Holthuijsen, L. H., and H. L. Tolman, 1991: Effects of the Gulf Stream on ocean waves. *J. Geophys. Res.*, **96**, 12755–12771, <https://doi.org/10.1029/91JC00901>.
- Hughes, B. A., 1978: The effect of internal waves on surface wind waves 2. Theoretical analysis. *J. Geophys. Res.*, **83**, 455–465, <https://doi.org/10.1029/JC083iC01p00455>.
- Kuik, A. J., G. P. van Vledder, and L. H. Holthuijsen, 1988: A method for the routine analysis of pitch-and-roll buoy wave data. *J. Phys. Oceanogr.*, **18**, 1020–1034, [https://doi.org/10.1175/1520-0485\(1988\)018<1020:AMFTRA>2.0.CO;2](https://doi.org/10.1175/1520-0485(1988)018<1020:AMFTRA>2.0.CO;2).
- Lenain, L., and N. Pizzo, 2021: Modulation of surface gravity waves by internal waves. *J. Phys. Oceanogr.*, **51**, 2735–2748, <https://doi.org/10.1175/JPO-D-20-0302.1>.
- Lewis, M. J., T. Palmer, R. Hashemi, P. Robins, A. Saulter, J. Brown, H. Lewis, and S. Neill, 2019: Wave-tide interaction modulates nearshore wave height. *Ocean Dyn.*, **69**, 367–384, <https://doi.org/10.1007/s10236-018-01245-z>.

- Longuet-Higgins, M. S., 1986: Eulerian and Lagrangian aspects of surface waves. *J. Fluid Mech.*, **173**, 683–707, <https://doi.org/10.1017/S0022112086001325>.
- , and R. W. Stewart, 1960: Changes in the form of short gravity waves on long waves and tidal currents. *J. Fluid Mech.*, **8**, 565–583, <https://doi.org/10.1017/S0022112060000803>.
- , and —, 1962: Radiation stress and mass transport in gravity waves, with application to ‘surf beats.’ *J. Fluid Mech.*, **13**, 481–504, <https://doi.org/10.1017/S0022112062000877>.
- Marechal, G., and F. Ardhuin, 2021: Surface currents and significant wave height gradients: Matching numerical models and high-resolution altimeter wave heights in the Agulhas Current region. *J. Geophys. Res. Oceans*, **126**, e2020JC016564, <https://doi.org/10.1029/2020JC016564>.
- Masson, D., 1996: A case study of wave–current interaction in a strong tidal current. *J. Phys. Oceanogr.*, **26**, 359–372, [https://doi.org/10.1175/1520-0485\(1996\)026<0359:ACSOWI>2.0.CO;2](https://doi.org/10.1175/1520-0485(1996)026<0359:ACSOWI>2.0.CO;2).
- McArthur, C. J., and M. Parsons, 2009: Ocean current and wave measurements at the Jacksonville and Fernandina Beach ocean dredged material disposal sites: August 2006 through September 2007. U.S. Environmental Protection Agency Region 4 EPA Tech. Rep. EPA-904-R-09-001, 70 pp., [https://www.epa.gov/sites/default/files/2017-02/documents/jacksonville\\_fernbeach\\_odmds\\_current\\_wave\\_study2010\\_1.pdf](https://www.epa.gov/sites/default/files/2017-02/documents/jacksonville_fernbeach_odmds_current_wave_study2010_1.pdf).
- Mei, C. C., 1992: *The Applied Dynamics of Ocean Surface Waves*. Advanced Series on Ocean Engineering, Vol. 1, World Scientific, 768 pp.
- , M. Stiassnie, and D. K.-P. Yue, 2005: *Theory and Applications of Ocean Surface Waves*. Advanced Series on Ocean Engineering, Vol. 23, World Scientific, 1136 pp.
- Merrifield, M. A., and Coauthors, 2021: An early warning system for wave-driven coastal flooding at Imperial Beach, CA. *Nat. Hazards*, **108**, 2591–2612, <https://doi.org/10.1007/s11069-021-04790-x>.
- NOAA, 2014: Continuously Updated Digital Elevation Model (CUDEM)—1/9 arc-second resolution bathymetric–topographic tiles. NOAA National Centers for Environmental Information, <https://doi.org/10.25921/ds9v-ky35>.
- O’Reilly, W. C., T. H. C. Herbers, R. J. Seymour, and R. T. Guza, 1996: A comparison of directional buoy and fixed platform measurements of Pacific swell. *J. Atmos. Oceanic Technol.*, **13**, 231–238, [https://doi.org/10.1175/1520-0426\(1996\)013<0231:ACODBA>2.0.CO;2](https://doi.org/10.1175/1520-0426(1996)013<0231:ACODBA>2.0.CO;2).
- Peregrine, D., 1976: Interaction of Water Waves and Currents. *Advances in Applied Mechanics*, Vol. 16, C.-S. Yih, Ed., Elsevier, 9–117, [https://doi.org/10.1016/S0065-2156\(08\)70087-5](https://doi.org/10.1016/S0065-2156(08)70087-5).
- Phillips, O. M., 1966: *The Dynamics of the Upper Ocean*. Cambridge University Press, 261 pp.
- , 1984: On the response of short ocean wave components at a fixed wavenumber to ocean current variations. *J. Phys. Oceanogr.*, **14**, 1425–1433, [https://doi.org/10.1175/1520-0485\(1984\)014<1425:OTROSO>2.0.CO;2](https://doi.org/10.1175/1520-0485(1984)014<1425:OTROSO>2.0.CO;2).
- Pizzo, N., and R. Salmon, 2021: Particle description of the interaction between wave packets and point vortices. *J. Fluid Mech.*, **925**, A32, <https://doi.org/10.1017/jfm.2021.661>.
- Pugh, D. T., 1987: *Tides, Surges and Mean Sea-Level*. John Wiley and Sons, 472 pp.
- Rasche, N., and F. Ardhuin, 2013: A global wave parameter database for geophysical applications. Part 2: Model validation with improved source term parameterization. *Ocean Modell.*, **70**, 174–188, <https://doi.org/10.1016/j.ocemod.2012.12.001>.
- Romero, L., L. Lenain, and W. K. Melville, 2017: Observations of surface wave–current interaction. *J. Phys. Oceanogr.*, **47**, 615–632, <https://doi.org/10.1175/JPO-D-16-0108.1>.
- , D. Hypolite, and J. C. McWilliams, 2020: Submesoscale current effects on surface waves. *Ocean Modell.*, **153**, 101662, <https://doi.org/10.1016/j.ocemod.2020.101662>.
- Shampine, L. F., and M. W. Reichelt, 1997: The MATLAB ODE suite. *SIAM J. Sci. Comput.*, **18**, 1–22, <https://doi.org/10.1137/S1064827594276424>.
- Tolman, H. L., 1988: Propagation of wind waves on tides. *21st Int. Conf. on Coastal Engineering*, Costa del Sol-Malaga, Spain, American Society of Civil Engineers, 512–523, <https://ascelibrary.org/doi/10.1061/9780872626874.037>.
- , 1990: The influence of unsteady depths and currents of tides on wind-wave propagation in shelf seas. *J. Phys. Oceanogr.*, **20**, 1166–1174, [https://doi.org/10.1175/1520-0485\(1990\)020<1166:TIOUDA>2.0.CO;2](https://doi.org/10.1175/1520-0485(1990)020<1166:TIOUDA>2.0.CO;2).
- , 1991: A third-generation model for wind waves on slowly varying, unsteady, and inhomogeneous depths and currents. *J. Phys. Oceanogr.*, **21**, 782–797, [https://doi.org/10.1175/1520-0485\(1991\)021<0782:ATGMFW>2.0.CO;2](https://doi.org/10.1175/1520-0485(1991)021<0782:ATGMFW>2.0.CO;2).
- , and N. Booij, 1998: Modeling wind waves using wavenumber-direction spectra and a variable wavenumber grid. *Global Atmos. Ocean Syst.*, **6**, 295–309.
- Unna, P. J. H., 1942: Waves and tidal streams. *Nature*, **149**, 219–220, <https://doi.org/10.1038/149219a0>.
- Vincent, C. E., 1979: The interaction of wind-generated sea waves with tidal currents. *J. Phys. Oceanogr.*, **9**, 748–755, [https://doi.org/10.1175/1520-0485\(1979\)009<0748:TIOWGS>2.0.CO;2](https://doi.org/10.1175/1520-0485(1979)009<0748:TIOWGS>2.0.CO;2).
- Vrećica, T., N. Pizzo, and L. Lenain, 2022: Observations of strongly modulated surface wave and wave breaking statistics at a submesoscale front. *J. Phys. Oceanogr.*, **52**, 289–304, <https://doi.org/10.1175/JPO-D-21-0125.1>.
- Wang, P., and J. Sheng, 2018: Tidal modulation of surface gravity waves in the Gulf of Maine. *J. Phys. Oceanogr.*, **48**, 2305–2323, <https://doi.org/10.1175/JPO-D-17-0250.1>.
- Wolf, J., and D. Prandle, 1999: Some observations of wave-current interaction. *Coastal Eng.*, **37**, 471–485, [https://doi.org/10.1016/S0378-3839\(99\)00039-3](https://doi.org/10.1016/S0378-3839(99)00039-3).